

# Triggering a global density wave instability in graphene via local symmetry-breaking

A. C. Qu<sup>1,2</sup>, P. Nigge<sup>1,2</sup>, S. Link<sup>3</sup>, G. Levy<sup>1,2</sup>, M. Michiardi<sup>1,2,4</sup>, P. L. Spandar<sup>5</sup>,  
T. Matthé<sup>1,2</sup>, M. Schneider<sup>1,2</sup>, S. Zhdanovich<sup>1,2</sup>, U. Starke<sup>3</sup>, C. Gutiérrez<sup>\*1,2,5</sup>, and  
A. Damascelli<sup>†1,2</sup>

<sup>1</sup>Department of Physics and Astronomy, University of British Columbia, Vancouver, Canada

<sup>2</sup>Quantum Matter Institute, University of British Columbia, Vancouver, Canada

<sup>3</sup>Max Planck Institute for Solid State Research, Stuttgart, Germany

<sup>4</sup>Max Planck Institute for the Physics of Complex Systems, Dresden, Germany

<sup>5</sup>Department of Physics and Astronomy, University of California, Los Angeles, Los Angeles, USA

**Two-dimensional quantum materials offer a robust platform for investigating the emergence of symmetry-broken ordered phases owing to the high tuneability of their electronic properties. For instance, the ability to create new electronic band structures in graphene through moiré superlattices from stacked and twisted structures has led to the discovery of several correlated and topological phases. Here we report an alternative method to induce an incipient symmetry-broken phase in graphene at the millimetre scale. We show that an extremely dilute concentration ( $< 0.3\%$ ) of surface adatoms can self-assemble and trigger the collapse of the graphene atomic lattice into a distinct Kekulé bond density wave phase, whereby the carbon C-C bond symmetry is broken globally. Using complementary momentum-resolved techniques such as angle-resolved photoemission spectroscopy (ARPES) and low-energy electron diffraction (LEED), we directly probe the presence of this density wave phase and confirm the opening of an energy gap at the Dirac point. We further show that this Kekulé density wave phase occurs for various Fermi surface sizes and shapes, suggesting that this lattice instability is driven by strong electron-lattice interactions. Our results demonstrate that dilute concentrations of self-assembled adsorbed atoms offer an attractive alternative route towards designing novel quantum phases in two-dimensional materials.**

A charge density wave (CDW) is a phase of matter that features a spatially modulated electron charge alongside a periodic distortion of the crystal lattice (*1*). These spatial modulations break the translational symmetry of the host crystal, resulting in a reconstruction of the Fermi surface that can open energy gaps in the electronic spectrum. CDW phases have been found in a myriad of systems and can coexist or compete

---

\*gutierrez@physics.ucla.edu

†damascelli@physics.ubc.ca

with other correlated phases, such as superconducting and Mott insulating states (2–4). In one dimensional systems, CDW formation is typically thought to be driven primarily by a divergent electronic response to charge modulations with wavevector  $\delta q = 2k_F$  that connects (or nests) the two points of the Fermi surface (1, 5). However, the mechanisms for CDW formation in higher-dimensional systems, where Fermi surface nesting is imperfect, is still highly debated (6–8).

Graphene, the prototypical two-dimensional material, presents an ideal tuneable system for exploring CDW formation: (i) At zero doping, its Fermi “surface” consists of two perfectly nested points (K/K’) at its Brillouin zone (BZ) corners connected by wavevector  $\delta \mathbf{q} = \mathbf{K} - \mathbf{K}'$ ; (ii) it features strong electron-phonon coupling and soft K-point phonon and plasmon modes (9–12); and (iii) its charge density, and thus the size of the Fermi surface and the CDW nesting condition, can be tuned with electrostatic gating or substrate charge-transfer. Owing to these unique properties, and the four-fold degeneracy of its spin and valley degrees of freedom, graphene has been shown to host a plethora of ordered electronic phases. One such phase is the Kekulé distortion (13–17), a bond density wave phase that has been described as a Peierls-like (5) lattice instability intrinsic to systems with relativistic dispersions (13, 18, 19). Undistorted graphene is composed of a honeycomb lattice of carbon atoms that exhibits six-fold bond symmetry (Fig. 1A). Its low-energy band structure is described by two inequivalent and gapless Dirac cones at K/K’ (Fig. 1B). In the Kekulé phase, the bond symmetry breaks such that the unit cell is tripled in size (thin/thick bonds, Fig. 1C). The new commensurate ( $\sqrt{3} \times \sqrt{3}$ ) $R30^\circ$  bonding pattern can be centred at one of three equivalent carbon hollow sites—distinguished by the use of red-grey-blue (RGB) colour tiling in Fig. 1C—and reflects the particular phase of the Kekulé order parameter. This supercell causes the previously inequivalent Dirac cones at K/K’ to be connected by a reciprocal lattice vector, which leads to a Fermi surface reconstruction that folds each cone to the Kekulé BZ center at  $\Gamma$  (Fig. 1D). Importantly, different topological Kekulé phases are determined by the specific broken C-C bond symmetry: the “O”-shaped pattern (Fig. 1C) opens an energy gap of  $2\Delta_K$  at the Dirac point (13, 14, 20) (Fig. 1D), while other “Y”-shaped patterns are gapless (21–25). When additionally allowing for a possible A-B sublattice symmetry breaking term,  $\Delta_{AB}$ , the total low-energy Kekulé dispersion is given by (26) (Methods):

$$\varepsilon(k) = \pm \sqrt{\hbar^2 v_F^2 k^2 + \Delta_{AB}^2 + |\Delta_K|^2}, \quad (1)$$

where  $\hbar$  is Planck’s constant divided by  $2\pi$ ,  $v_F$  is the Fermi velocity, and  $k$  is the crystal momentum.

To date there have been few direct experimental observations of the graphene Kekulé phase (20, 23, 27, 28). In theory, it can arise through several mechanisms: electron-electron (12, 14, 17) and electron-phonon interactions (13, 15, 29, 30); from high-density ( $\sqrt{3} \times \sqrt{3}$ ) $R30^\circ$  adatom superlattices (22, 28, 31–33); and large biaxial strain (34, 35). The nature of the Kekulé phase is of fundamental interest as it provides an example of spontaneous gap formation via K/K’ valley (“chiral”) symmetry breaking (15, 16, 26, 36), and it has been predicted to host topological defects with fractionalized charge (14). Most recently, Kekulé lattice instabilities have attracted attention as candidates for the correlated insulating states in twisted bilayer graphene (37–41). Here we report a controllable method for inducing the Kekulé density wave phase in graphene via the deposition of an extremely dilute concentration of lithium adatoms. Using angle-resolved photoemission spectroscopy (ARPES) (42) we probe the electronic band structure of this density wave phase and directly image the folded Dirac cones at the BZ center, as well as observe the opening of an energy gap of  $2\Delta_K \approx 200$  meV at the Dirac point, the two signatures of the Kekulé-O phase in graphene.

We induce the Kekulé-O phase (henceforth simply referred to as Kekulé) in graphene through electron-mediated self-assembly of lithium (Li) adatoms. Adatoms on graphene can scatter electrons between valleys K

and  $K'$ , producing unique long-range Friedel oscillations with a hexagonal  $(\sqrt{3} \times \sqrt{3})R30^\circ$  pattern and period determined by scattering wavevectors that satisfy the Kekulé nesting condition  $\delta\mathbf{q} = \mathbf{K} - \mathbf{K}'$  (43–47). Each Li adatom site thus nucleates a local patch of Kekulé density wave order of radius  $\sim 2\text{--}5$  nm (46), resulting in symmetry breaking between the three previously equivalent RGB Kekulé “colours” (Fig. 1E,F). Other mobile Li adatoms interact with the long-range  $(\sqrt{3} \times \sqrt{3})R30^\circ$  charge modulations, preferring an arrangement that allows their Friedel oscillations to be in phase (Fig. 1G). The constructive interference between several adatom-induced oscillations on a single “colour” site produces enhanced charge-density modulations and, through electron-phonon coupling, the emergence of the Kekulé distortion throughout graphene—even when the adatoms themselves may be many unit cells apart (Fig. 1H) (44, 45). The adatoms are said to observe hidden Kekulé order, since without the RGB colour scheme, the long-range adatom ordering would be obscured (44, 45).

In Fig. 2A we show ARPES data from pristine monolayer epitaxial graphene on silicon carbide (Gr/SiC) (48) (Methods). ARPES energy-momentum maps are plotted along the yellow cut in momentum space shown in Fig. 2C, at the graphene K point. Due to charge-transfer from the substrate, the Dirac point is shifted to  $\approx 430$  meV below the Fermi level  $E_F$  (48–50). The observed intensity asymmetry of the two branches of the Dirac cone in Fig. 2A is due to the experimental geometry and the polarisation of the ultraviolet light source (51). Momentum distribution curves (MDCs) at each binding energy are fit with two Lorentzians, whose peak positions are indicative of the electronic dispersions of the conduction and valence bands (thick yellow lines, 2A). Close to the Fermi energy, the dispersions are well described by linear fits (thin yellow lines, 2A) above and below the Dirac point at  $-430$  meV binding energy. For massless Dirac fermions, the extrapolated fits from the two energy bands would cross at the Dirac point. Such crossing, however, is not observed. The origin of this apparent energy gap has been attributed to a sublattice symmetry breaking term ( $\Delta_{AB}$  in Eq. 1) (49, 52) or band renormalization due to electron-plasmon effects (50). As we describe below, the precise microscopic origin of the pre-existing gap in pristine Gr/SiC is not crucial to our findings, and in either picture our results are qualitatively the same. In order to extract energy gap values, we employ the sublattice symmetry breaking picture which allows us to model our experimental data with a simple tight-binding Hamiltonian (Methods). This analysis yields an energy gap of  $2\Delta = (292 \pm 4)$  meV at the Dirac point (25). Importantly, for pristine graphene near  $E_F$ , there is no ARPES intensity at  $\Gamma$ , the BZ centre.

Having confirmed the electronic structure for pristine graphene, we next decorate its surface with Li adatoms. Due to electron charge transfer from Li, the Dirac point is expected to shift downward in binding energy with increased Li concentration (25, 31–33, 53). However, we observe only a negligible shift of the Dirac point (below our 20 meV energy resolution), as shown by a direct comparison of ARPES intensity before (Fig. 2A) and after (Fig. 2B) Li deposition. We conclude that an extremely low Li surface coverage is achieved, with a conservative estimate of less than 0.3%, corresponding to an average Li-Li distance of  $\geq 2$  nm (Methods). Despite this negligible change in charge density, we observe that the measured energy gap at the Dirac point increases by 20% to  $2\Delta' = 354 \pm 2$  meV. Since Li adatoms occupy graphene sublattice symmetric hollow sites (Fig. 1E) (31), Li cannot further break A-B sublattice symmetry. Additionally, this gap enhancement after ultra low 0.3% Li deposition cannot be explained by electron-plasmon effects (25). As we will show below, we attribute this increased gap to the onset of Kekulé density wave order. From Eq. (1), Dirac point energy gaps from concomitant sublattice symmetry breaking and Kekulé order add in quadrature,  $2\Delta' = 2\sqrt{\Delta_{AB}^2 + \Delta_K^2}$ , which in our measurements corresponds to  $2\Delta_K \approx 200$  meV. More striking, and the primary signature of Kekulé order, is the appearance of new electronic energy bands centred at the  $\Gamma$  point,

and directly observed in Fermi surface maps (Fig. 2C). These new bands appear as a replica Dirac cone (Fig. 2D), which we interpret as the Kekulé-induced superposition of folded Dirac cones at K and K', as in Fig. 1D. This is supported by the momentum-symmetric intensity of the Dirac cone centred at  $\Gamma$  (Fig. 2D), which reflects its mixed K/K' character (Fig. 2B) due to contributions from Dirac cones at opposite ends of the graphene BZ (Fig. 2C, red hexagon). By performing a similar MDC analysis on this new Dirac cone at  $\Gamma$ , we extract a larger energy gap opening of  $2\Delta' = 377 \pm 2$  meV in contrast to the gap observed at the BZ corner. A possible explanation for this discrepancy is that measurements at  $\Gamma$  exclusively probe areas with the gapped Kekulé distorted phase, while those measured at K probe areas with both distorted and undistorted graphene.

Similar band folding and gap opening behaviour has been observed in previous experiments where alkali atoms were intercalated into bilayer graphene at a high density (33%, or 100 times our estimated Li concentration) (28, 32, 33). However, in these experiments, band folding is naturally expected to occur owing to the presence of the uniform  $(\sqrt{3} \times \sqrt{3})R30^\circ$  adatom superlattice potential that explicitly breaks the translational symmetry of graphene. Additionally, this high adatom coverage strongly electron-dopes graphene, resulting in a significant shift of the Dirac point ( $\sim 1$  eV) (32, 53, 54) and the appearance of additional alkali atom-derived electronic bands at  $\Gamma$  (31, 53). We detect no such Dirac point shift nor additional Li-derived bands. In contrast, our results are well explained by the global onset of an incipient and phase-coherent Kekulé density wave instability driven by the long-range ordering of an extremely dilute ( $< 0.3\%$ ) concentration of mobile Li adatoms (44, 45). This is especially evidenced by the particular sharpness of the replica Dirac cone at  $\Gamma$  (Figs. 2D–E) over the large spot size of our ultraviolet light source ( $\sim 1$  mm). This long range phase coherence originates from a majority of mobile Li adatoms occupying a single-coloured Kekulé site (Fig. 1H); and it is confirmed by additional temperature-dependent measurements (up to 30 K), which found that the folded  $\Gamma$ -point Dirac bands surprisingly sharpen further as the sample is warmed, indicative of increased hidden Kekulé order as more single-coloured Kekulé sites are populated by mobile Li adatoms (25). Notably, while natural point defects have been shown to nucleate density wave order in bulk materials (55, 56), this is the first controlled demonstration of dilute extrinsic adatoms inducing a global density wave phase in a two-dimensional material.

We note that such direct signatures of density wave order in monolayer graphene are rare (23, 27). As charge density waves are concomitant with periodic lattice distortions (1), a Kekulé distortion of the graphene lattice (Fig. 1C) should be reflected in diffraction measurements. To further support our claim of a global Kekulé distorted phase, we performed *in situ* low temperature low-energy electron diffraction (LEED) measurements (spot size  $\sim 1$  mm) (Fig. 3). Before Li deposition, the pristine surface displays sharp diffraction peaks characteristic of epitaxial graphene grown on SiC (Fig. 3A). After dilute Li deposition, new and sharp diffraction peaks appear corresponding to a well-defined and long-ranged  $(\sqrt{3} \times \sqrt{3})R30^\circ$  lattice (Fig. 3B). Relative to the atomic graphene Bragg peaks (red arrows, Fig. 3C), the new diffraction peaks (blue arrows, Fig. 3C) have intensities of  $\sim 20\%$  with similar peak widths (25). In light of the ultra-dilute surface coverage of Li adatoms ( $< 0.3\%$ ), the intensity and sharpness of these new diffraction peaks points to the presence of a globally well-defined Kekulé lattice distortion in graphene.

We next present a simple model that captures how the emergence of Kekulé order depends on the two key control parameters in our study: sample temperature and Li deposition rate. In our experiments, we find that Kekulé order occurs only when (i) Li is deposited with graphene held at low temperature ( $< 10$  K) and (ii) Li is deposited at a slow rate. We employ a kinetic hopping model that incorporates the graphene-

mediated long-range interaction between Li adatoms on graphene (Fig. 1E–H), which is attractive for Li located on Kekulé RGB lattices sites of the same “colour” and repulsive otherwise (44, 45) (see (25) for detailed discussion). In the model (Fig. 4A), Li can hop to neighbouring sites with a Boltzmann probability dependent on temperature and the local Kekulé-modulated potential energy landscape created by all other surface Li atoms (Fig. 4C). We quantify the strength of RGB Kekulé order in the system by calculating the magnitude of the  $(\sqrt{3}\times\sqrt{3})R30^\circ$  Fourier component of the Li lattice positions. In agreement with our findings, slower Li deposition (Fig. 4A) produces coherent long-range Kekulé order across the entire sample, while faster deposition (Fig. 4B) only permits order on the scale of a few sites. By performing several simulations with varying temperatures and deposition rates (Fig. 4D), we find that long-range Kekulé ordering does not form at high sample temperatures. The unique combination of slow deposition at low temperature in our experiments may explain why Kekulé order in dilute Li graphene systems has not been reported previously (53). However, starting from the ordered phase, higher temperature can initially improve long-range Kekulé order via increased Li mobility (Fig. S10) until the kinetic energy eclipses the Kekulé confining potential (Fig. 4C), whence Li hopping becomes random and destroys the ordered phase (25).

Thus far, our results are well explained by the predictions of hidden Kekulé ordering of adatoms (44, 45). A key parameter for long-range Li order is the graphene doping level: At finite charge density, additional Friedel oscillations of magnitude  $2k_F$  (43, 45–47) contribute to the scattered wavevector and disrupt the perfect nesting condition (fig. S9,  $\delta\mathbf{q} = \mathbf{K} - \mathbf{K}' + 2\mathbf{k}_F$ ). When the charge density becomes larger than the density of Li adatoms that nucleate local Kekulé order,  $n_e > n_{\text{Li}}$ , the  $2k_F$  charge modulations effectively randomize the sign of the interaction between Li adatoms at distances  $\ell_{\text{Li}} > 1/\sqrt{n_e}$  (44, 45). Large charge densities are thus expected to destroy any long range Li order, preventing the formation of a global, phase coherent Kekulé distortion. To test this electronic density dependence, we measured two additional epitaxial monolayer graphene samples with different doping levels (Fig. 5). Photoemission spectra from hydrogen (H) and gadolinium (Gd) intercalated graphene-SiC measured at the graphene K point are shown in Figs. 5A and C, respectively. The H-intercalated sample (Gr/H/SiC) is *p*-doped (57), with the Dirac point shifted to  $\sim 100$  meV above  $E_F$ , while the Gd-intercalated sample (Gr/Gd/SiC) is strongly *n*-doped (54) with the Dirac point shifted to  $\sim 1.6$  eV below  $E_F$ . Figures 5B and D display ARPES measurements at  $\Gamma$  after Li deposition at low temperature and deposition rate. Surprisingly, we again find signatures of Kekulé distortion-induced folded K/K' Dirac cones at  $\Gamma$ . The folded nature of the bands is especially apparent for Gr/Gd/SiC at ultra-high electron density ( $n_e > 10^{14}$  cm $^{-2}$ ), where we can directly visualize different portions of the trigonal-warped Fermi surface using different light polarisations (58) (Fig. 5E–G). Importantly, no ARPES intensity is present at  $\Gamma$  prior to Li deposition.

Despite significant differences in the size and carrier type of the Fermi surfaces, we observe signatures of Li-induced Kekulé distortion across all three graphene systems. While understanding the microscopic origin of this Kekulé ordering and its robustness to variation in the electron density will require more theoretical work, the role of Fermi surface nesting in the global lattice distortion can be tentatively ruled out. An alternative, promising mechanism is momentum-dependent electron-phonon coupling, which has been found to drive lattice distortions in other 2D systems (6, 7); indeed, electron-phonon coupling is strong in graphene, and especially so for the K-point  $A'_1$  “breathing” mode phonon (9–11), which has the exact symmetry as the Kekulé distortion (Fig. 1C) and its dispersion,  $\Omega_{A'_1}(\mathbf{q})$ , displays a strong renormalisation (Kohn anomaly) at the Kekulé wavevector. This hypothesis could be further explored via time-resolved ARPES experiments, which can extract the mode-projected electron-coupling value (11) before and after the Kekulé distortion is

induced.

Interestingly, Kekulé order and other coherent valley-coupled states have been theorized (37–41, 59) to explain the correlated insulating and superconducting states in magic angle twisted bilayer graphene (60–62). However, a microscopic origin of the proposed global intervalley-coupling is yet to be determined. Detailed phonon calculations on relaxed twisted bilayer structures showed that localized Kekulé order can emerge near moiré AA stacking sites, opening unexpectedly large gaps in the flat band energy spectrum (59). Defect-induced global Kekulé distortion may thus provide a plausible microscopic mechanism for the valley-coupling in twisted bilayer graphene. Most importantly, our results show that even an extremely dilute concentration of atomic-scale defects can initiate the global onset of an incipient density wave instability in pristine monolayer graphene.

### Acknowledgements

The authors acknowledge useful discussions with J. H. Smet, A. Kogar, R. M. Fernandes, Z.-B. Kang, and I. F. Herbut. **Funding:** This research was undertaken thanks in part to funding from the Max Planck-UBC-UTokyo Centre for Quantum Materials and the Canada First Research Excellence Fund, Quantum Materials and Future Technologies Program. The work at UBC was supported by the Killam, Alfred P. Sloan, and Natural Sciences and Engineering Research Council of Canada’s (NSERC’s) Steacie Memorial Fellowships (A.D.), the Alexander von Humboldt Fellowship (A.D.), the Canada Research Chairs Program (A.D.), NSERC, Canada Foundation for Innovation (CFI), British Columbia Knowledge Development Fund (BCKDF), and the CIFAR Quantum Materials Program. Work at MPI Stuttgart was supported by the German Research Foundation (DFG) in the framework of the Priority Program No. 1459, Graphene (Sta315/8-2). **Author contributions:** A.C.Q. and P.N. performed the ARPES and LEED experiments and analyzed the ARPES data. S.L. and U.S. grew all graphene samples. A.C.Q. performed tight binding calculations. A.C.Q. developed the thermal atomic hopping model and performed calculations with assistance from T. M. P.L.S. and C.G. analyzed LEED data. A.C.Q., P.N., M.M., M.S., S.Z., and G.L. provided technical support and maintenance for the ARPES setup. C.G. and A.D. supervised the project. A.C.Q. and C.G. wrote the manuscript with input from all authors. A.D. was responsible for overall project direction, planning, and management. **Competing interests:** The authors declare no competing financial interest.

## REFERENCES AND NOTES

1. G. Grüner, *Density Waves in Solids* (Addison-Wesley, 1994).
2. D. E. Moncton, J. D. Axe, F. J. DiSalvo, Neutron scattering study of the charge-density wave transitions in  $2H\text{-TaSe}_2$  and  $2H\text{-NbSe}_2$ . *Phys. Rev. B* **16**, 801–819 (2 1977).
3. J. Tranquada, B. Sternlieb, J. Axe, Y. Nakamura, S. Uchida, Evidence for stripe correlations of spins and holes in copper oxide superconductors. *Nature* **375**, 561–563 (1995).
4. B. Sipos, A. F. Kusmartseva, A. Akrap, H. Berger, L. Forró, E. Tutiš, From Mott state to superconductivity in  $1T\text{-TaS}_2$ . *Nat. Mater.* **7**, 960–965 (2008).
5. R. E. Peierls, *Quantum Theory of Solids* (Clarendon Press, 1956).
6. M. D. Johannes, I. I. Mazin, Fermi surface nesting and the origin of charge density waves in metals. *Phys. Rev. B* **77**, 165135 (16 2008).

7. F. Weber, S. Rosenkranz, J.-P. Castellan, R. Osborn, R. Hott, R. Heid, K.-P. Bohnen, T. Egami, A. H. Said, D. Reznik, Extended Phonon Collapse and the Origin of the Charge-Density Wave in  $2H-NbSe_2$ . *Phys. Rev. Lett.* **107**, 107403 (10 2011).
8. X. Zhu, Y. Cao, J. Zhang, E. Plummer, J. Guo, Classification of charge density waves based on their nature. *Proc. Natl. Acad. Sci.* **112**, 2367–2371 (2015).
9. S. Piscanec, M. Lazzeri, F. Mauri, A. C. Ferrari, J. Robertson, Kohn Anomalies and Electron-Phonon Interactions in Graphite. *Phys. Rev. Lett.* **93**, 185503 (2004).
10. S. Y. Zhou, D. A. Siegel, A. V. Fedorov, A. Lanzara, Kohn anomaly and interplay of electron-electron and electron-phonon interactions in epitaxial graphene. *Phys. Rev. B* **78**, 193404 (19 2008).
11. M. Na, A. K. Mills, F. Boschini, M. Michiardi, B. Nosarzewski, R. P. Day, E. Razzoli, A. Sheyerman, M. Schneider, G. Levy, *et al.*, Direct determination of mode-projected electron-phonon coupling in the time domain. *Science* **366**, 1231–1236 (2019).
12. T. Tudorovskiy, S. A. Mikhailov, Intervalley plasmons in graphene. *Phys. Rev. B* **82**, 073411 (7 2010).
13. C. Chamon, Solitons in carbon nanotubes. *Phys. Rev. B* **62**, 2806–2812 (2000).
14. C.-Y. Hou, C. Chamon, C. Mudry, Electron Fractionalization in Two-Dimensional Graphenelike Structures. *Phys. Rev. Lett.* **98**, 186809 (2007).
15. K. Nomura, S. Ryu, D.-H. Lee, Field-Induced Kosterlitz-Thouless Transition in the  $N = 0$  Landau Level of Graphene. *Phys. Rev. Lett.* **103**, 216801 (2009).
16. I. F. Herbut, V. Jurić, B. Roy, Theory of interacting electrons on the honeycomb lattice. *Phys. Rev. B* **79**, 085116 (8 2009).
17. C. Weeks, M. Franz, Interaction-driven instabilities of a Dirac semimetal. *Phys. Rev. B* **81**, 085105 (Feb. 2010).
18. A. V. Balatsky, Peierls instability and chiral-symmetry breaking in solids with “relativistic” fermions. *Phys. Rev. Lett.* **64**, 2078–2081 (1990).
19. J. W. Mintmire, B. I. Dunlap, C. T. White, Are fullerene tubules metallic? *Phys. Rev. Lett.* **68**, 631–634 (5 1992).
20. K. K. Gomes, W. Mar, W. Ko, F. Guinea, H. C. Manoharan, Designer Dirac fermions and topological phases in molecular graphene. *Nature* **483**, 306–310 (2012).
21. M. Koshino, T. Morimoto, M. Sato, Topological zero modes and Dirac points protected by spatial symmetry and chiral symmetry. *Phys. Rev. B* **90**, 115207 (11 2014).
22. Y. Ren, X. Deng, Z. Qiao, C. Li, J. Jung, C. Zeng, Z. Zhang, Q. Niu, Single-valley engineering in graphene superlattices. *Phys. Rev. B* **91**, 245415 (24 2015).
23. C. Gutiérrez, C.-J. Kim, L. Brown, T. Schiros, D. Nordlund, E. B. Lochocki, K. M. Shen, J. Park, A. N. Pasupathy, Imaging chiral symmetry breaking from Kekulé bond order in graphene. *Nat. Phys.* **12**, 950–958 (May 2016).
24. O. V. Gamayun, V. P. Ostroukh, N. V. Gnezdilov, I. Adagideli, C. W. J. Beenakker, Valley-momentum locking in a graphene superlattice with Y-shaped Kekulé bond texture. *New J. Phys.* **20**, 023016 (2018).
25. See supplementary materials.

26. S. Ryu, C. Mudry, C.-Y. Hou, C. Chamon, Masses in graphenelike two-dimensional electronic systems: Topological defects in order parameters and their fractional exchange statistics. *Phys. Rev. B* **80**, 205319 (2009).
27. S.-Y. Li, Y. Zhang, L.-J. Yin, L. He, Scanning tunneling microscope study of quantum Hall isospin ferromagnetic states in the zero Landau level in a graphene monolayer. *Phys. Rev. B* **100**, 085437 (8 2019).
28. C. Bao, H. Zhang, T. Zhang, X. Wu, L. Luo, S. Zhou, Q. Li, Y. Hou, W. Yao, L. Liu, P. Yu, J. Li, W. Duan, H. Yao, Y. Wang, S. Zhou, Experimental Evidence of Chiral Symmetry Breaking in Kekulé-Ordered Graphene. *Phys. Rev. Lett.* **126**, 206804 (2021).
29. M. Kharitonov, Phase diagram for the  $\nu = 0$  quantum Hall state in monolayer graphene. *Phys. Rev. B* **85**, 155439 (2012).
30. L. Classen, M. M. Scherer, C. Honerkamp, Instabilities on graphene's honeycomb lattice with electron-phonon interactions. *Phys. Rev. B* **90**, 035122 (2014).
31. M. Farjam, H. Rafii-Tabar, Energy gap opening in submonolayer lithium on graphene: Local density functional and tight-binding calculations. *Phys. Rev. B* **79**, 045417 (2009).
32. K. Sugawara, K. Kanetani, T. Sato, T. Takahashi, Fabrication of Li-intercalated bilayer graphene. *AIP Advances* **1**, 022103 (Apr. 2011).
33. K. Kanetani, K. Sugawara, T. Sato, R. Shimizu, K. Iwaya, T. Hitosugi, T. Takahashi, Ca intercalated bilayer graphene as a thinnest limit of superconducting  $C_6Ca$ . *Proc. Natl. Acad. Sci.* **109**, 19610 (2012).
34. C. A. Marianetti, H. G. Yevick, Failure Mechanisms of Graphene under Tension. *Phys. Rev. Lett.* **105**, 245502 (2010).
35. S.-H. Lee, H.-J. Chung, J. Heo, H. Yang, J. Shin, U.-I. Chung, S. Seo, Band gap opening by two-dimensional manifestation of Peierls instability in graphene. *ACS Nano* **5**, 2964–2969 (2011).
36. V. Gusynin, S. Sharapov, J. Carbotte, AC conductivity of graphene: From tight-binding model to 2 + 1-dimensional quantum electrodynamics. *Int. J. Mod. Phys. B* **21**, 4611–4658 (2007).
37. X. Y. Xu, K. T. Law, P. A. Lee, Kekulé valence bond order in an extended Hubbard model on the honeycomb lattice with possible applications to twisted bilayer graphene. *Phys. Rev. B* **98**, 121406 (12 2018).
38. A. Thomson, S. Chatterjee, S. Sachdev, M. S. Scheurer, Triangular antiferromagnetism on the honeycomb lattice of twisted bilayer graphene. *Phys. Rev. B* **98**, 075109 (7 2018).
39. Y. Da Liao, Z. Y. Meng, X. Y. Xu, Valence bond orders at charge neutrality in a possible two-orbital extended Hubbard model for twisted bilayer graphene. *Phys. Rev. Lett.* **123**, 157601 (2019).
40. S.-M. Huang, Y.-P. Huang, T.-K. Lee, Slave-rotor theory on magic-angle twisted bilayer graphene. *Phys. Rev. B* **101**, 235140 (23 2020).
41. Y. Da Liao, J. Kang, C. N. Breiø, X. Y. Xu, H.-Q. Wu, B. M. Andersen, R. M. Fernandes, Z. Y. Meng, Correlation-Induced Insulating Topological Phases at Charge Neutrality in Twisted Bilayer Graphene. *Phys. Rev. X* **11**, 011014 (1 2021).
42. A. Damascelli, Probing the electronic structure of complex systems by ARPES. *Phys. Scr.* **T109**, 61–74 (2004).



43. V. V. Cheianov, V. I. Fal'ko, Friedel Oscillations, Impurity Scattering, and Temperature Dependence of Resistivity in Graphene. *Phys. Rev. Lett.* **97**, 226801 (22 Nov. 2006).
44. V. Cheianov, V. Fal'ko, O. Syljuåsen, B. Altshuler, Hidden Kekulé ordering of adatoms on graphene. *Solid State Commun.* **149**, 1499–1501 (2009).
45. V. V. Cheianov, O. Syljuåsen, B. L. Altshuler, V. Fal'ko, Ordered states of adatoms on graphene. *Phys. Rev. B* **80** (Dec. 2009).
46. G. M. Rutter, J. Crain, N. Guisinger, T. Li, P. First, J. Stroscio, Scattering and interference in epitaxial graphene. *Science* **317**, 219–222 (2007).
47. P. Mallet, I. Brihuega, S. Bose, M. M. Ugeda, J. M. Gomez-Rodriguez, K. Kern, J.-Y. Veuillen, Role of pseudospin in quasiparticle interferences in epitaxial graphene probed by high-resolution scanning tunneling microscopy. *Phys. Rev. B* **86**, 045444 (2012).
48. S. Forti, U. Starke, Epitaxial graphene on SiC: from carrier density engineering to quasi-free standing graphene by atomic intercalation. *J. Phys. D: Appl. Phys.* **47**, 094013 (2014).
49. S. Y. Zhou, G.-H. Gweon, A. V. Fedorov, P. N. First, W. A. de Heer, D.-H. Lee, F. Guinea, A. H. C. Neto, A. Lanzara, Substrate-induced bandgap opening in epitaxial graphene. *Nat. Mater.* **6**, 770–775 (Sept. 2007).
50. A. Bostwick, T. Ohta, T. Seyller, K. Horn, E. Rotenberg, Quasiparticle dynamics in graphene. *Nat. Phys.* **3**, 36–40 (2007).
51. I. Gierz, J. Henk, H. Höchst, C. R. Ast, K. Kern, Illuminating the dark corridor in graphene: Polarization dependence of angle-resolved photoemission spectroscopy on graphene. *Phys. Rev. B* **83**, 121408 (12 2011).
52. P. Nigge, A. Qu, É. Lantagne-Hurtubise, E. Mårzell, S. Link, G. Tom, M. Zonno, M. Michiardi, M. Schneider, S. Zhdanovich, *et al.*, Room temperature strain-induced Landau levels in graphene on a wafer-scale platform. *Sci. Adv.* **5**, eaaw5593 (2019).
53. B. M. Ludbrook, G. Levy, P. Nigge, M. Zonno, M. Schneider, D. J. Dvorak, C. N. Veenstra, S. Zhdanovich, D. Wong, P. Dosanjh, C. Straßer, A. Stöhr, S. Forti, C. R. Ast, U. Starke, A. Damascelli, Evidence for superconductivity in Li-decorated monolayer graphene. *Proc. Natl. Acad. Sci.* **112**, 11795–11799 (2015).
54. S. Link, S. Forti, A. Stöhr, K. Küster, M. Rösner, D. Hirschmeier, C. Chen, J. Avila, M. C. Asensio, A. A. Zakharov, T. O. Wehling, A. I. Lichtenstein, M. I. Katsnelson, U. Starke, Introducing strong correlation effects into graphene by gadolinium intercalation. *Phys. Rev. B* **100**, 121407 (12 2019).
55. A. V. Melechko, J. Braun, H. H. Weitering, E. W. Plummer, Two-Dimensional Phase Transition Mediated by Extrinsic Defects. *Phys. Rev. Lett.* **83**, 999–1002 (1999).
56. C. J. Arguello, S. P. Chockalingam, E. P. Rosenthal, L. Zhao, C. Gutiérrez, J. Kang, W. Chung, R. M. Fernandes, S. Jia, A. J. Millis, *et al.*, Visualizing the charge density wave transition in  $2H$ -NbSe<sub>2</sub> in real space. *Phys. Rev. B* **89**, 235115 (2014).
57. C. Riedl, C. Coletti, T. Iwasaki, A. A. Zakharov, U. Starke, Quasi-Free-Standing Epitaxial Graphene on SiC Obtained by Hydrogen Intercalation. *Phys. Rev. Lett.* **103**, 246804 (24 2009).

58. S. W. Jung, S. H. Ryu, W. J. Shin, Y. Sohn, M. Huh, R. J. Koch, C. Jozwiak, E. Rotenberg, A. Bostwick, K. S. Kim, Black phosphorus as a bipolar pseudospin semiconductor. *Nat. Mater.* **19**, 277–281 (2020).
59. M. Angeli, E. Tosatti, M. Fabrizio, Valley Jahn-Teller effect in twisted bilayer graphene. *Phys. Rev. X* **9**, 041010 (2019).
60. Y. Cao, V. Fatemi, A. Demir, S. Fang, S. L. Tomarken, J. Y. Luo, J. D. Sanchez-Yamagishi, K. Watanabe, T. Taniguchi, E. Kaxiras, R. C. Ashoori, P. Jarillo-Herrero, Correlated insulator behaviour at half-filling in magic-angle graphene superlattices. *Nature* **556**, 80–84 (2018).
61. Y. Cao, V. Fatemi, S. Fang, K. Watanabe, T. Taniguchi, E. Kaxiras, P. Jarillo-Herrero, Unconventional superconductivity in magic-angle graphene superlattices. en, *Nature* **556**, 43–50 (Apr. 2018).
62. L. Balents, C. R. Dean, D. K. Efetov, A. F. Young, Superconductivity and strong correlations in moiré flat bands. *Nat. Phys.* **16**, 725–733 (2020).

## Figures

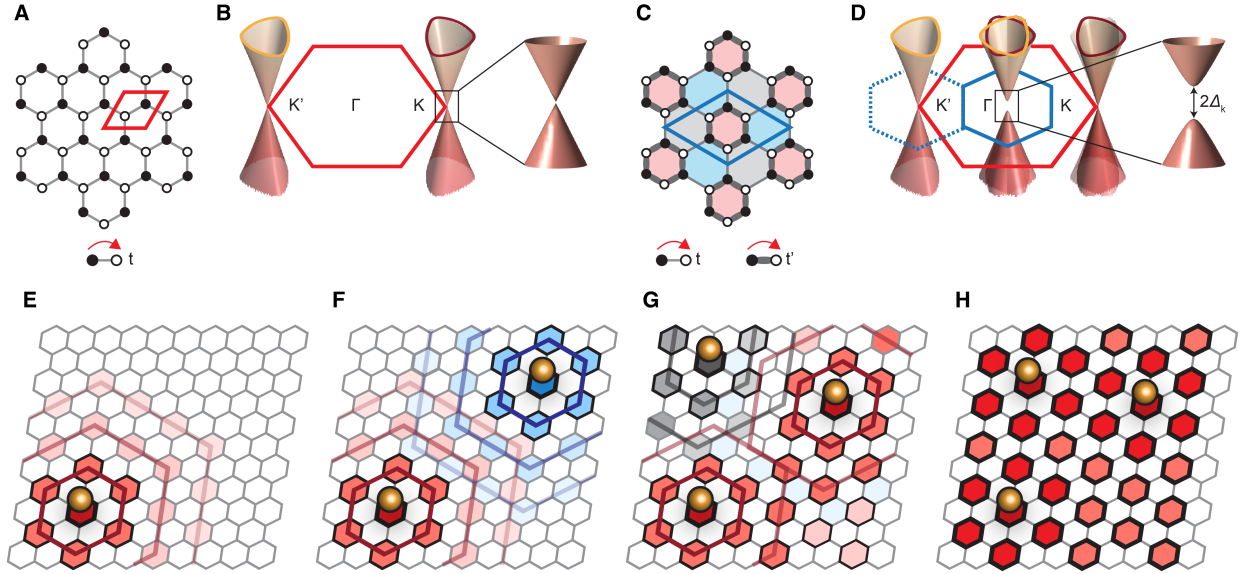


Figure 1: **The Kekulé phase and hidden Kekulé ordering of lithium on graphene.** **A**, Schematic diagram of pristine graphene. The red diamond indicates the primitive unit cell. All bonds between adjacent atoms are equivalent owing to the same hopping energy,  $t$ . **B**, Schematic diagram of the graphene band structure composed of two gapless Dirac cones  $K/K'$  located at the corners of the Brillouin zone (red hexagon). **C**, Schematic diagram of Kekulé distorted graphene. The bond symmetry breaks (thin, thick lines) owing to new hopping energies ( $t, t'$ ), forming a  $(\sqrt{3} \times \sqrt{3})R30^\circ$  superstructure and tripling the size of the unit cell (blue diamond). The supercell can be visualized by the red-grey-blue colouring of the three inequivalent hexagonal plaquettes. **D**, The superstructure leads to a smaller Brillouin zone (blue hexagon) and the  $K/K'$  Dirac cones being folded to  $\Gamma$ , as well as a gap opening at the Dirac point. At energies above the Dirac point, the folded trigonal bands intersect, producing a Star of David pattern. The intensity of folded bands at  $K/K'$  is exaggerated for clarity. **E**, A single adatom on graphene produces Friedel oscillations with a local  $(\sqrt{3} \times \sqrt{3})R30^\circ$  structure on a red site. Bond distortions (thick lines) appear near the adatom. **F-H**, Additional adatoms produce their own Friedel oscillations on out-of-phase sites (blue, gray). The mobile adatoms interact through their Friedel oscillations, preferring to occupy red sites where the oscillations interfere constructively. Hidden Kekulé order occurs when a majority of adatoms occupy one of the RGB sites, inducing the Kekulé distortion globally.

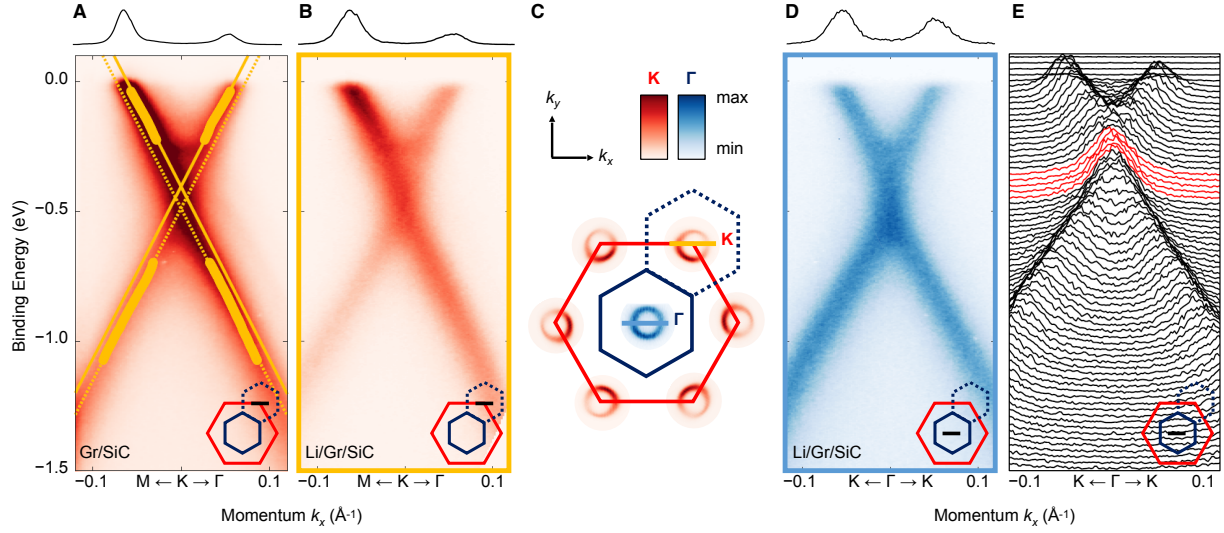


Figure 2: **Lithium-induced Kekulé bond density wave formation in graphene.** **A**, ARPES spectra of pristine graphene on SiC through the Dirac cone at K (cut indicated by yellow line in **C**). The Dirac cone displays electron doping due to charge transfer from the substrate, and one branch appears brighter due to matrix element effects. This is shown in the momentum distribution curve (MDC) at the Fermi level (top). MDC peak positions are indicated by thick yellow lines; linear fits through the top (solid lines) and bottom (dotted lines) indicate the presence of an energy gap (see text). **B**, The same spectra as **A** after dilute Li deposition. No charge transfer doping from Li is detectable. **C**, Schematic of the Brillouin zones of pristine graphene (red) and  $(\sqrt{3} \times \sqrt{3})R30^\circ$  Kekulé graphene (blue) superimposed on the Fermi surfaces as observed by ARPES (not to scale, see Fig. S9). Locations of the ARPES cuts in **A–B** and **D–E** are indicated by the yellow and blue lines, respectively. **D**, ARPES spectra at  $\Gamma$  (cut indicated by blue line in **C**) after lithium deposition. The two Dirac cones at K/K' are folded to  $\Gamma$ . Both branches are equally bright, indicating the mixed K/K' character of the bands as shown in the Fermi level MDC (top). **E**, MDCs of the spectra shown in **D**. Fits to MDC curves reveal an energy gap at the Dirac point (25). The spectra in red lie inside the gap region.

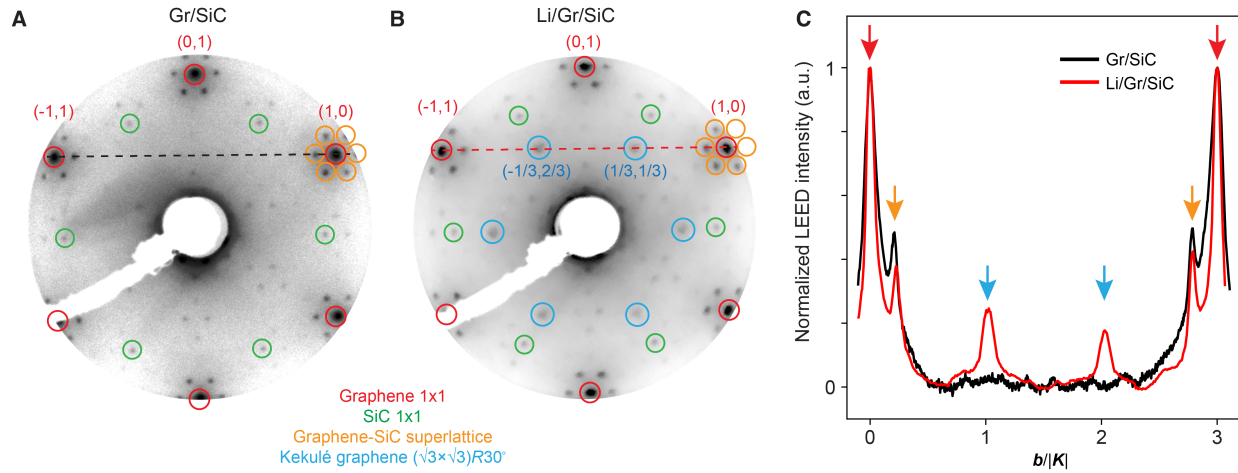


Figure 3: **Low energy electron diffraction (LEED) of graphene in the Kekulé phase.** **A**, LEED pattern measured at 66 eV on pristine Gr/SiC. Peaks are highlighted with circles corresponding to graphene (red), SiC (green), and the graphene/SiC superlattice pattern (yellow). **B**, LEED pattern after dilute lithium deposition at low temperature. New diffraction spots corresponding to  $(\sqrt{3} \times \sqrt{3})R30^\circ$  Kekulé bond order (blue) are clearly visible. **C**, Line profiles along the black (red) dotted line in **A** (**B**) after subtraction of a smooth background (25). The horizontal axis is in units of the K-point wavevector,  $|\mathbf{K}|=1.70 \text{ \AA}^{-1}$ . Diffraction peaks are indicated by arrows using the same colour scheme used in **B**. The width of the graphene and graphene/SiC peaks are comparable before and after Li deposition. The new Kekulé diffraction peaks (blue arrows) are intense ( $\sim 20\%$ ) and as sharp as the graphene Bragg peaks (red arrows), indicating long-range Kekulé bond order.

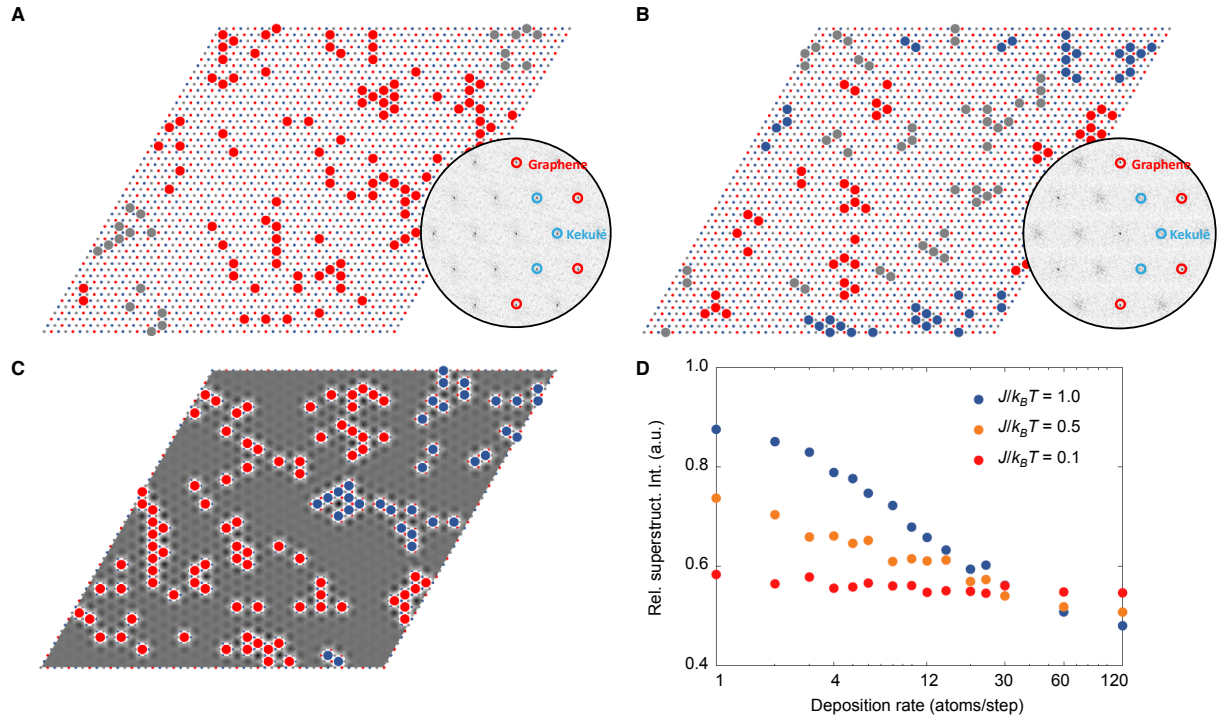


Figure 4: **Kinetic model for hidden Kekulé ordering of Li.** **A**, Simulation of 120 adatoms (large dots) added randomly one at a time (slow deposition) to red, grey, or blue (RGB) hollow sites that form three  $(\sqrt{3} \times \sqrt{3})R30^\circ$  mosaic Kekulé lattices on graphene. After each Li is added, the adatoms interact through a long range “ferromagnetic”-like potential (see main text) and the system is evolved thermally (25). The formation of a large unicolour (red) Kekulé order is observed. Inset: Fourier transform of the simulation, with sharp peaks at the  $(\sqrt{3} \times \sqrt{3})R30^\circ$  Kekulé ordering wavevector signifying long-range order. **B**, Final state of a similar simulation when adatoms are added in a single step (fast deposition) and allowed to evolve thermally. Unicolour patches are much smaller than those from slow deposition in **A**, and the Kekulé peaks in the Fourier transform are broadened, signifying short-range order. **C**, Simulated potential energy landscape originating from the superposition of  $(\sqrt{3} \times \sqrt{3})R30^\circ$  Friedel oscillations from all adatoms. The egg carton-like potential is deepest (dark) near large unicolour regions, where mobile adatoms can become “trapped” and further enhance the Kekulé order. **D**, Intensity of the Fourier peak corresponding to the  $(\sqrt{3} \times \sqrt{3})R30^\circ$  Kekulé lattice (normalized by the intensity at the graphene Bragg peak) as a function of adatom deposition rate, for different values of  $J/k_B T$ , where  $J$  is the adatom-adatom interaction coupling constant (see (25)),  $k_B$  is the Boltzmann constant, and  $T$  is temperature. At low temperatures ( $J/k_B T \geq 1$ ), Kekulé order is strongest for slow adatom deposition; at high temperatures ( $J/k_B T \ll 1$ ), Kekulé order is weak at any deposition rate.

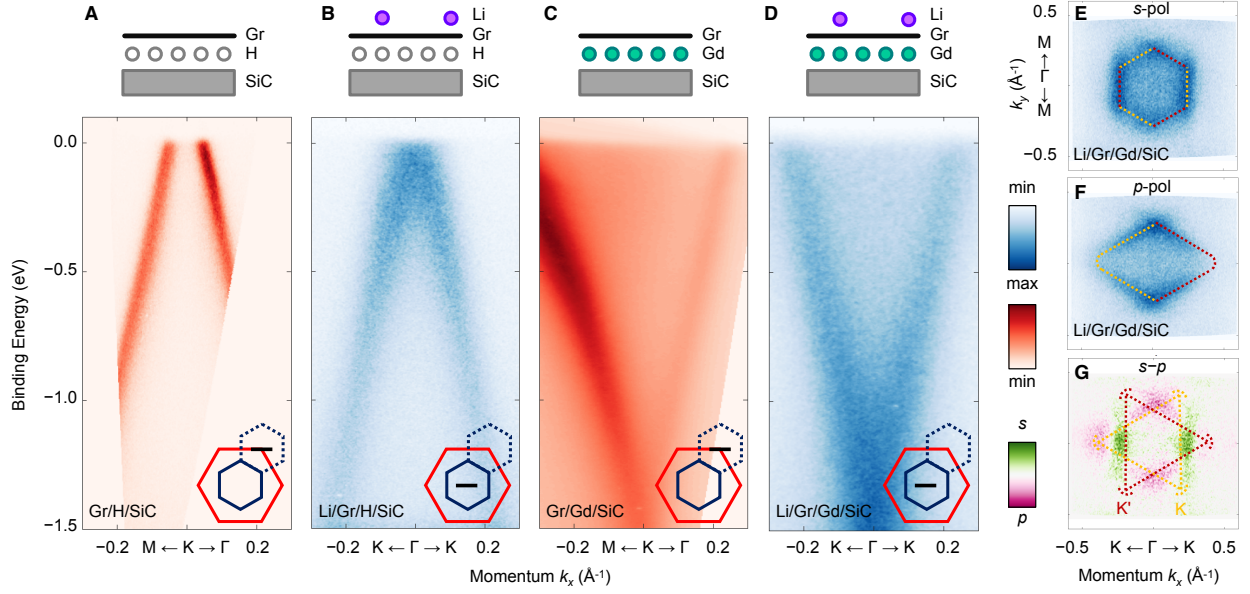


Figure 5: **Li-induced Kekulé phase in different graphene systems.** **A**, ARPES spectra taken at the K point (cut indicated by inset) on hydrogen-intercalated graphene (Gr/H/SiC) (sample schematic is shown above the cut). The Dirac point is located  $\sim 100$  meV above  $E_F$ . **B**, Spectra at  $\Gamma$  on Gr/H/SiC after lithium deposition showing the folded Dirac cone due to Kekulé distortion. **C**, Spectra at K on gadolinium-intercalated graphene (Gr/Gd/SiC). Graphene is strongly doped with the Dirac point located  $\sim 1.6$  eV below  $E_F$ . **D**, Spectra at  $\Gamma$  on Gr/Gd/SiC after lithium deposition showing the folded Dirac cone. The folded Dirac cones in **B** and **D** display bands with symmetric intensities, signifying a folding of the two Dirac cones at K/K'. **E**, Fermi surface of Gr/Gd/SiC at  $\Gamma$  after Li deposition using *s*-polarized light. A schematic of the bands expected to be visible in this configuration is overlaid in yellow and red dotted lines. **F**, The same Fermi surface as in **E** using *p*-polarized light. **G**, Difference map between **E** and **F**. A schematic of the trigonal-warped Fermi surfaces folded from K and K' is overlaid in yellow (K) and red (K') dotted lines.